XI. PLASMA MAGNETOHYDRODYNAMICS AND ENERGY CONVERSION[*]

Prof. G. A. Brown
Prof. R. S. Cooper
Prof. W. H. Heiser
Prof. M. A. Hoffman
Prof. W. D. Jackson
Prof. J. L. Kerrebrock
Prof. J. E. McCune
Prof. G. C. Oates
Prof. E. S. Pierson
Prof. A. H. Shapiro
Prof. R. E. Stickney

Dr. J. B. Heywood
J. L. Coggins
R. Dethlefsen
K. R. Edwards
J. W. Gadzuk
T. K. Gustafson
R. F. Keating
R. W. King
G. B. Kliman
A. G. F. Kniazzeh
R. M. Logan
B. T. Lubin

M. A. Lutz
C. A. McNary
R. P. Porter
S. Sacks
C. V. Smith, Jr.
A. Solbes
R. J. Thome
B. D. Wessler
J. C. Wissmiller
S. Yamamoto
G. W. Zeiders

A. CONDENSING EJECTOR TEST FACILITY

A flexible test facility is now under construction for use on basic research on high-performance condensing ejectors for liquid-metal MHD power systems. The test facility is shown schematically in Fig. XI-1. Steam passes from the laboratory main through a flowmetering section and enters the steam side of the stagnation tank where the pressure and temperature are measured. Water from the city supply passes through a centrifugal pump, a flowmetering section and enters the water side of the stagnation tank where the pressure and temperature are measured. The outlet end of the stagnation tank contains separate nozzle passages in which the steam and water are accelerated. Upon leaving the nozzles, the streams come in contact in the convergent portion of the mixing section and then flow into the constant-area portion of the mixing section. After the mixing process has been completed, the condensed stream of liquid enters a diffuser section and is discharged through a back-pressure control valve, a condenser-cooler, and to the laboratory canal system. Pressure instrumentation will be provided along the length of the mixing section and the diffuser. The stagnation pressure and temperature at the exit of the diffuser will also be measured. A condenser cooler has been provided in the flow loop, since it is possible that a flashing process will occur as the liquid is throttled through the back-pressure control valve leading to steam in the discharge lines. Since the water in the laboratory canal system must be maintained at approximately constant temperature, the condenser cooler will be used to condense any steam and cool the exit stream from the diffuser to the desired temperature.

Figure XI-2 shows the stagnation tank with the front cover removed. Water enters the stagnation tank through the rear cover and along the center line of the tank. The
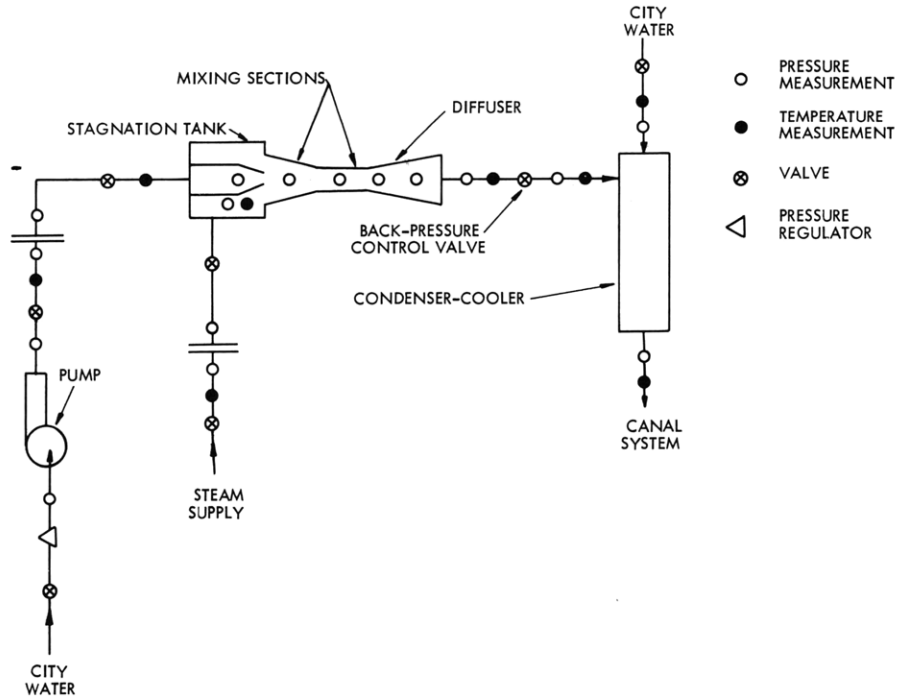
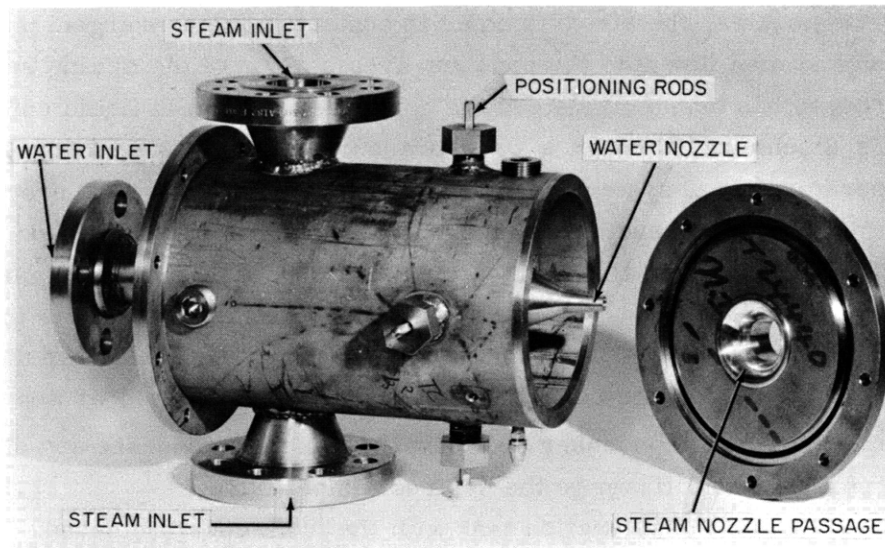Fig. XI-1. Schematic diagram of the condensing ejector test facility.

Fig. XI-2. Stagnation tank system (cover off).

passage which serves as a steam nozzle is formed by the outer wall of the water nozzle and a contoured section which is attached to the front cover of the stagnation tank (see Fig. XI-2). The shape of the steam nozzle can obviously be varied by selecting appropriate contours for the two walls comprising the steam nozzle.

Four positioning rods have been placed in the walls of the stagnation tank in order to locate the water nozzle concentrically with respect to the mixing sections that will be attached to the front cover of the stagnation tank. Aligning plugs that can be inserted through the mixing section and fit around the outer tip of the water nozzle have been machined. The water nozzle will be positioned approximately, and the aligning plug then inserted. Once proper alignment has been established, the positioning rods will be locked. This procedure is considered to be critical, since many of the convergent mixing sections will have an exit area that is only slightly larger than the exit area of the water nozzle. Inaccurate alignment of the water nozzle could, therefore, lead to impingement of the water jet on the walls of the mixing section with an accompanying adverse loss in momentum.

Figure XI-3 shows the stagnation tank with the front cover in place. The mixing section flange located in this cover can also be seen. The rear side of this flange contains the outer contour of the steam nozzle. The front side of the flange, which is
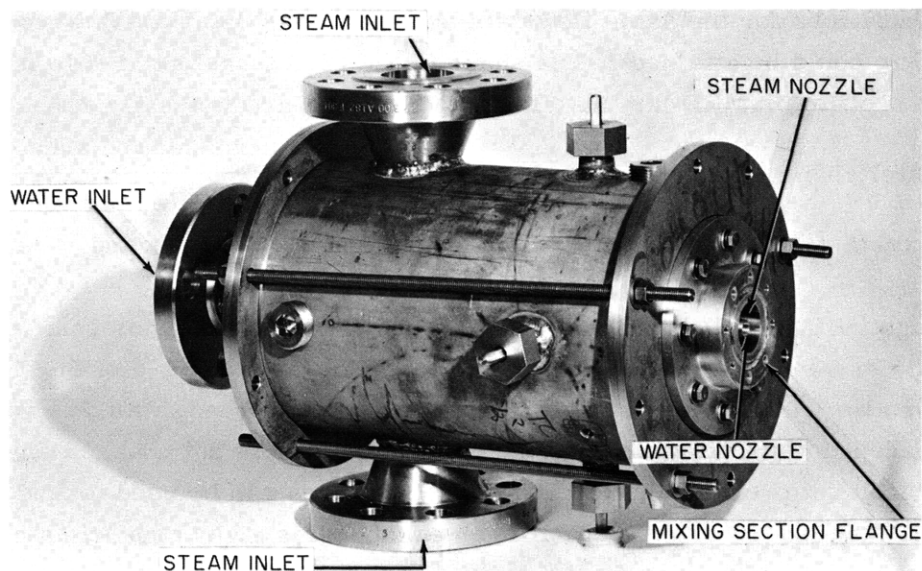

Fig. XI-3. Stagnation tank system (cover on).

visible in Fig. XI-3, will be used to attach mixing sections of various shapes to the stagnation tank. The mixing sections will be constructed either from metal materials for high-pressure operation or high-temperature transparent plastic materials in order to view the flow pattern.

G. A. Brown

B. BOUNDARY-LAYER ANALYSIS OF TURBULENT MAGNETOHYDRODYNAMIC CHANNEL FLOWS

The flow in a practical MHD (magnetohydrodynamic) machine will probably be turbulent because of the large velocities and Reynolds numbers, R_e, required to obtain a reasonable power density. Laminar-flow analysis is important because turbulent flow is not susceptible to the same kind of analysis; solutions have not been obtained even for the simplest ordinary hydrodynamic (OHD) channel flows; however, it does not replace the missing turbulent-flow solutions. Since little information, either experimental or theoretical, is now available on MHD turbulent flows, boundary-layer theory is used as an approximate technique for determining the effect of turbulence and the turbulent velocity profile on the I^2R losses caused by circulating currents and the viscous losses. This has been established as a valuable technique for handling OHD flows, and is useful for MHD flows.

In turbulent flow the simple picture of laminar flow or flow in layers is no longer valid. Instead there is violent eddying and momentum transfer in the direction perpendicular to the average flow; this has the effect of averaging the velocities or reducing the velocity gradient over the central part of the flow. Near the walls there are sharp gradients, since the wall velocity is zero. This flow pattern causes a marked increase in the viscous loss for the same flow rate over that with laminar-flow conditions (if laminar flow could be attained). The shape of the OHD turbulent profile is similar to the Hartmann profile for MHD laminar flow. OHD flows are normally turbulent for $R_e = \dfrac{\rho \bar{v} D_h}{\eta}$ greater than approximately 2000, where $D_h = 4 \dfrac{\text{(cross-section area of flow)}}{\text{(wetted perimeter)}}$ is the hydraulic diameter, ρ and η are the fluid density and viscosity, and $\bar{v}$ is the average velocity.

Although OHD turbulent channel flow has not yielded to analysis, sufficient experimental data are available to obtain a good picture of the structure of the flow and the velocity profile. In the limit of small electromagnetic forces, which is not of practical interest except in MHD flowmeters, the velocity profile is not changed significantly from the OHD turbulent profile, and the known OHD profiles can be used to find the electromagnetic fields and powers for an MHD machine. This gives approximate results, but is not valid for design purposes.

The interaction of a transverse DC magnetic field with a turbulent flow has been studied experimentally[1-3] and theoretically,[4] but the present available information is of limited value. Only experimental measurements of friction factor or pressure drop are available, with no way to separate the contribution resulting from circulating currents from the viscous loss. In machine analysis the circulating current loss is included separately, so that only the viscous loss is desired. Harris[4] has studied turbulent MHD

flows using semiempirical techniques. He obtained an equation for the friction factor for the total pressure drop (plotted in Fig. XI-5) and derived a theoretical time-average velocity profile, both for no external electrical connection to the fluid. There is some question as to the general validity of his results, as his friction-factor predictions do not extrapolate from the earlier data to fit a more recent experiment.[3] Experimental studies of velocity profiles are needed.

The situation is more complex with an AC or traveling magnetic field, and there are no experimental results for either case. The pulsating electromagnetic force will probably decrease the stability of laminar flow, and possibly increase the turbulent losses.

1. Boundary-Layer Theory

In boundary-layer theory the fluid flow is split into two parts: (i) a region near the wall in which viscosity is important, and where there are large velocity gradients normal to the wall; and (ii) a region away from the wall where viscous forces are negligible, no large velocity gradients occur, and the flow is essentially potential flow. The flow can be solved by assuming an inviscid fluid and potential flow to determine the gross behavior; and then viscosity is considered only in the thin layer along the body because the fluid velocity is zero at the wall.

In OHD flows the viscous forces in the boundary layer are balanced by inertial forces. The fluid slows down, and the boundary-layer thickness must grow along the surface to satisfy conservation of momentum. For channel flow the boundary layers will grow from the entrance until they meet, after which the viscous force is balanced by the pressure gradient, so that boundary-layer theory is valid only for determining the entry length.

In MHD channel flow electromagnetic terms are added to the force balance, and this allows the thickness of the boundary layer to stabilize at some finite value. If the boundary-layer thickness δ is small compared with the channel half-width a, the channel flow can be represented by a central core in which the velocity is constant and the electromagnetic force balances the pressure gradient, and a thin boundary layer in which viscosity and velocity gradients are important. This description bears a qualitative relation to Hartmann flow, and the analytical results are similar.

Boundary-layer theory is introduced in OHD flow because exact or approximate solutions can be obtained for cases in which the complete Navier-Stokes equation cannot be solved. It can be applied to laminar flow directly, and to turbulent flow with the use of experimental measurements. Two approaches are available: a differential form obtained from the Navier-Stokes equation with small terms neglected, and an integral form as used here. The differential form is used for laminar flow to obtain the velocity profile in the boundary layer and the boundary-layer thickness, but solutions are difficult to obtain even for simple geometries, and only a few solutions are available. The integral form neglects the details of the boundary layer; a velocity profile is assumed, and δ is determined as a function of this velocity profile. The results for this approximate method are within a few per cent for OHD laminar flows, as shown by Schlichting.[5] For

turbulent flows insufficient knowledge is available to use the differential form, and the integral form can be solved only with the aid of experimental data. For a thorough discussion of boundary-layer theory applied to OHD flows, see Schlichting.[6]
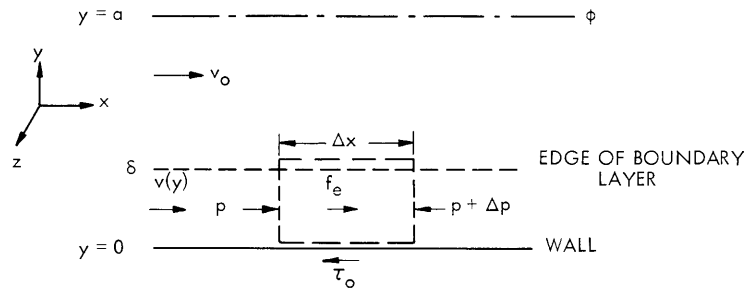

Fig. XI-4. Model for boundary-layer analysis.

The integral form of the force-balance equation for the boundary layer is obtained by using the model of Fig. XI-4. The x-directed forces acting on the small volume are the wall shear stress τ_o, the pressure gradient, and the electromagnetic force f_{ex}. Only the constant boundary layer, δ independent of x, is considered, so that there is no net transport of momentum into the volume. Since the fluid velocity in the central region is a constant, v_o, no shear stress acts on the upper surface of the volume. The force equation in the x-direction, with the limit taken as $\Delta x \rightarrow 0$, is

$$\tau_o + \int_0^\delta \frac{\partial p}{\partial x} dy - \int_0^\delta f_{ex}\, dy = 0 \tag{1}$$

for a unit length in the z-direction and no dependence on z. The force balance equation for the whole channel, also required, is written by using symmetry about the center. Cancelling out the part contained in the boundary-layer equation leaves

$$\int_\delta^a \frac{\partial p}{\partial x} dy - \int_\delta^a f_{ex}\, dy = 0. \tag{2}$$

This determines the pressure, which is then eliminated from Eq. 1.

The solution depends on the type of machine. For an MHD induction machine, treated here as an example, the time-average force[7,8] is

$$f_{ex} = \frac{\eta(v_s - v)\, M^2}{a^2}, \tag{3}$$

where

$$M^2 = \frac{\sigma a^2}{\eta} \frac{|B_y|^2}{2} \tag{4}$$

is the Hartmann number based on the rms transverse magnetic field, σ is the fluid conductivity, a is the channel half-height in the y-direction, v is the fluid velocity, and v_s is the velocity of the traveling magnetic field. In general, B_y or M will vary across the channel, so that it is necessary to consider the dependence of $\partial p / \partial x$ on y. In this case the velocity should vary across the channel as in laminar flow,[7,8] and the constant-velocity core is not a good assumption. It has been shown that the only case of interest for a practical machine is a narrow channel,[7,8] where B_y and M are constant. Restricting attention to this case, the time-average pressure gradient is

$$\left\langle \frac{\partial p}{\partial x} \right\rangle = \frac{\eta}{a^2} (v_s - v_o) \, M^2 \qquad (5)$$

from Eq. 2, and the equation to solve is

$$\frac{\tau_o}{\eta} + \frac{M^2}{a^2} \left[\int_0^\delta v \, dy - v_o \delta \right] = 0. \qquad (6)$$

For a DC machine with a transverse magnetic field, f_{ex} depends on M^2 and the voltage difference between the electrodes, but the analysis is similar to the induction machine.

2. Laminar Flow

For laminar flow, the wall shear stress is

$$\tau_o = \eta \left. \frac{dv}{dy} \right|_{y=0}. \qquad (7)$$

The velocity profiles tested are the linear, second-order, third-order, etc., profiles, and a sinusoidal profile. The boundary conditions are that the velocity is zero at y = 0 and v_o at y = δ for all profiles, and the higher order profiles have the proper number of zero derivatives at y = δ. The profile equations in terms of the normalized dimension $\tilde{y} = \frac{y}{\delta}$, and the results for the normalized boundary-layer thickness $\frac{\delta}{a}$ and the normalized wall shear stress $[\tau_o / (\eta v_o / a)]$, which are proportional to $1/M$ and M, respectively, are given in Table 3.2.1.

A more convenient parameter than δ is the displacement thickness

$$\delta^* = \int_0^a \left(1 - \frac{v}{v_o} \right) dy, \qquad (8)$$

which is the distance the channel wall would have to be moved in to maintain the same volume flow rate if the velocity were constant at v_o. As the velocity profile becomes a better approximation and a smoother transition occurs at y = δ, $\delta \to \infty$ because the approach is asymptotic. This is not true for δ^*.

The displacement thickness and τ_o are also given for the Hartmann profile for M > 4, but δ is not defined, since the velocity approaches v_o asymptotically. Both δ^* and τ_o are

Table XI-1. δ, δ^*, and τ_o for a laminar boundary layer.

$\dfrac{v}{v_o}$	$\dfrac{(\delta/a)}{(1/M)}$	$\dfrac{(\delta^*/a)}{(1/M)} = \dfrac{[\tau_o/(\eta v_o/a)]}{M}$
$\tilde{y}$	$\sqrt{2} = 1.414$	$\sqrt{\dfrac{1}{2}} = 0.707$
$2\tilde{y} - \tilde{y}^2$	$\sqrt{6} = 2.449$	$\sqrt{\dfrac{2}{3}} = 0.816$
$3\tilde{y} - 3\tilde{y}^2 + \tilde{y}^3$	$\sqrt{12} = 3.464$	$\sqrt{\dfrac{3}{4}} = 0.866$
n^{th} order*	$\sqrt{(n+1)n}$	$\sqrt{\dfrac{n}{n+1}}$
$\sin\left(\dfrac{\pi}{2}\tilde{y}\right)$	$\sqrt{\dfrac{\pi^2}{2(\pi-2)}} = 2.085$	$\sqrt{\dfrac{\pi-2}{2}} = 0.749$
Hartmann, $M > 4$	—	1

*
$$\frac{v}{v_o} = n\tilde{y} - \frac{n(n-1)}{2!}\tilde{y}^2 + \frac{n(n-1)(n-2)}{3!}\tilde{y}^3 - \ldots + (-1)^{n-1}\tilde{y}^n$$

low for the boundary layer or approximate solutions, and approach the Hartmann solution only for large n. The variations among the boundary-layer solutions and the differences from the exact solution are worse than for the comparable OHD flow over a flat plate, in which these amount to only a few per cent.[5]

The laminar boundary-layer solution does not add to the methods available for treating MHD machines. It differs little from the Hartmann profile and approaches it for better approximations to the velocity profile in the boundary layer. The advantage of boundary-layer theory lies in treating turbulent flow, when other analytical methods are not applicable and experimental measurements are not available.

3. Turbulent Flow

The extension of boundary-layer theory to turbulent flow should include
(i)   The use of an MHD turbulent profile in the boundary layer.
(ii) The effect of turbulent flow on the wall shear stress.
(iii) The additional losses, both viscous and I^2R, caused by the turbulence.
(iv) The effect of the turbulent core on the boundary layer; that is, the momentum transfer from the core to the boundary layer, if any, and the change in the boundary conditions on the boundary layer caused by fluctuations in the core.[9]

In OHD turbulent boundary-layer theory the first three points are satisfied by using available experimental data. The fourth point is not well understood, and is generally neglected. Since suitable experiments for MHD flows are nonexistent, it is not possible to properly extend the MHD theory to cover turbulent flow. Instead, MHD turbulent flow can be treated approximately by using the OHD experimental results for the velocity profile and wall shear stress. The profile shape is wrong, but it is not too critical, provided δ^*/a is small. The I^2R turbulent loss, for which no OHD equivalent exists, is not included in this approach.

The $\left(\frac{1}{7}\right)^{th}$-power velocity profile and associated wall shear stress,[10]

$$\frac{v}{v_o} = \left(\frac{y}{\delta}\right)^{1/7} , \tag{9}$$

and

$$\tau_o = \rho v_o^2 (0.0225) \left(\frac{\eta}{\rho v_o \delta}\right)^{1/4} , \tag{10}$$

from experimental pipe flow data, are used as in OHD turbulent boundary layers. These are based on v_o and δ instead of v and a, as is the custom for pipe flow. This is valid for moderate Reynolds numbers. Better accuracy might be obtained from the "universal velocity distribution" law, but this is too complicated to use here.[11]

Rewriting Eq. 6 to include this profile and solving give

$$\frac{\delta}{a} = \frac{0.254}{M} \left(R_e^*\right)^{3/5} , \tag{11}$$

$$\tau_o = \left(\frac{\eta v_o}{a}\right) M(0.0317) \left(R_e^*\right)^{3/5} , \tag{12}$$

and

$$\delta^* = \frac{\delta}{8} , \tag{13}$$

where

$$R_e^* = \frac{\rho v_o}{\eta} \left(\frac{a}{M}\right) \tag{14}$$

is the Reynolds number based roughly on δ and v_o. Relating R_e^* to R_e by means of the ratio of the average to maximum velocities yields

$$R_e = R_e^*(4M) \left(1 - \frac{\delta^*}{a}\right). \tag{15}$$

Here R_e, the fundamental parameter, is determined by the flow independently of the actual profile. This theory is invalid if $\delta^*/a > 1$ (the boundary layers meet), and is

expected to be inaccurate if δ^*/a approaches 1. The range of applicability of the theory increases with M, since the larger electromagnetic force limits the spread of the boundary layer.

It is convenient for turbulent flows to use the friction factor, defined as $\dfrac{8\tau_o}{\rho v^2}$, to calculate the viscous pressure drop and power loss. For this theory it is

$$f = (0.254)\ \frac{1}{\left(1 - \dfrac{\delta^*}{a}\right)^2}\ \frac{1}{\left(R_e^*\right)^{2/5}}. \tag{16}$$

This does not include the pressure drop resulting from the I^2R losses in the fluid. A graph of f as a function of R_e for M = 100 is given in Fig. 3.2.2. Also shown are the friction factors for OHD turbulent flow,[12] and for DC MHD laminar and turbulent flows. Direct-current MHD flows are turbulent for $R_e/M > 900$, while induction-driven flows are probably turbulent for a smaller ratio. The MHD turbulent flow curve, obtained by
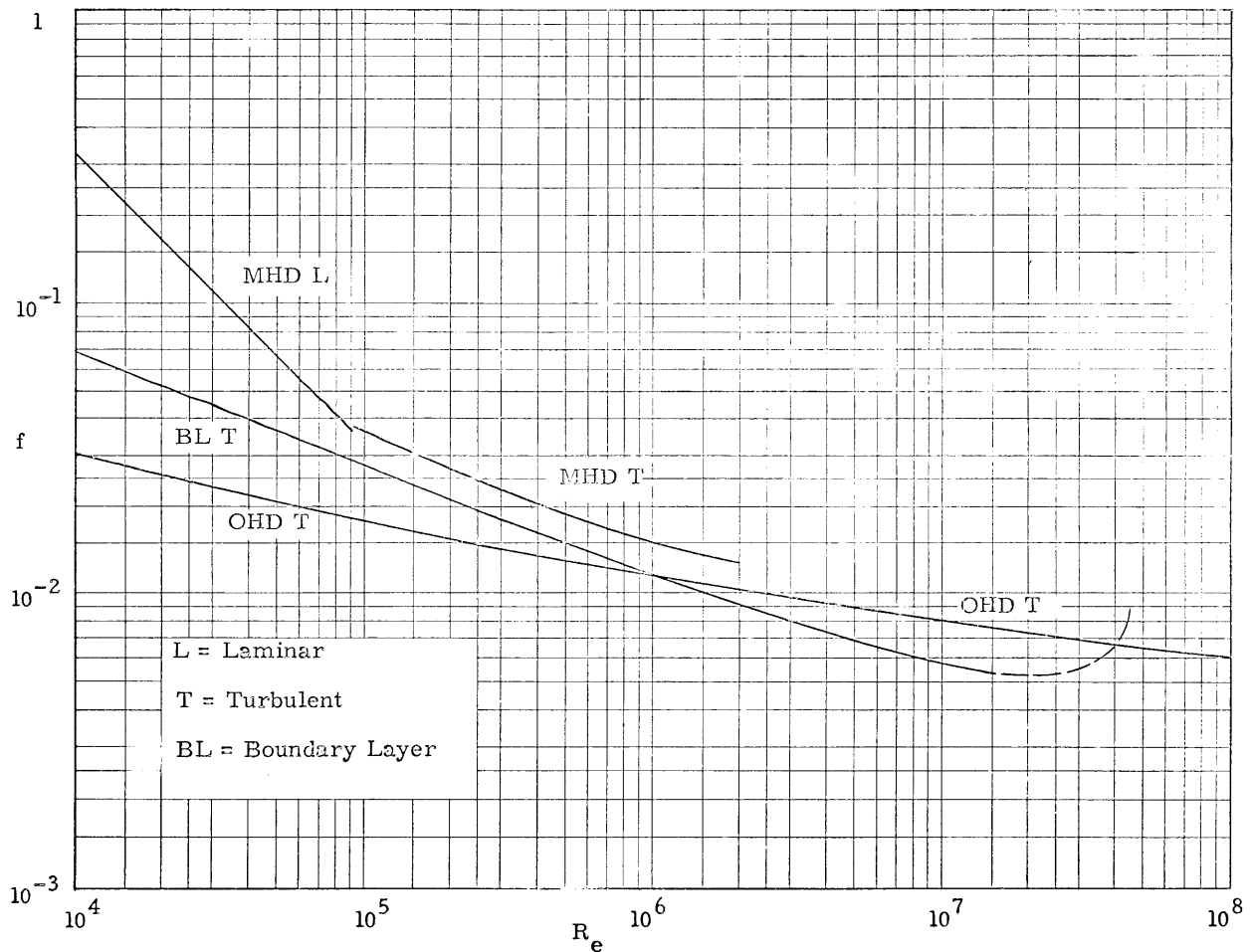

Fig. XI-5. Friction factors, M = 100.

Harris from experimental data,[13] is valid for $M^2/\sqrt{f}\,R_e > 0.053$, which leaves only a limited range of applicability.

The boundary-layer solution lies between the OHD and MHD turbulent curves. This is reasonable because MHD flows probably have a higher viscous loss than OHD flows, but the curve should lie below the experimental MHD curve which includes both viscous and I^2R losses. This solution breaks down, as we have mentioned, when δ^*/a comes close to 1, which occurs about where the friction-factor curve starts to turn up (shown dashed in Fig. XI-5). Similar curves are obtained for other values of M.

The OHD and MHD turbulent friction-factor curves cross for large R_e. It is questionable whether this will actually occur; further study is required.

It is not possible to estimate the accuracy of the MHD turbulent boundary-layer solution without experimental information. It does appear reasonable, however, when compared with the previous results for the friction factor. There is an urgent need for further experimental measurements on both DC and induction-coupled turbulent MHD flows.

E. S. Pierson

References

1. J. Hartmann and F. Lazarus, "Hg-Dynamics II," Kgl. Danske Videnskab. Selskab, Mat.-Fys. Medd. 15, 7 (1937).

2. W. Murgatroyd, "Experiments on Magneto-Hydrodynamic Channel Flow," Phil. Mag. 44, 1348-1354 (1953).

3. E. C. Brouillette and P. S. Lykoudis, "Measurements of Skin Friction for Turbulent Magnetofluidmechanic Channel Flow," Report No. A and ES 62-10, School of Aeronautical and Engineering Sciences, Purdue University, 1962.

4. L. P. Harris, Hydromagnetic Channel Flows (John Wiley and Sons, Inc., New York, 1960).

5. H. Schlichting, Boundary Layer Theory (McGraw-Hill Book Company, New York, 1960), pp. 238-243.

6. Ibid.

7. E. S. Pierson, "The MHD Induction Machine," Sc. D. Thesis, Department of Electrical Engineering, Massachusetts Institute of Technology, Cambridge, Massachusetts, 1964, Chapter 4.

8. E. S. Pierson and W. D. Jackson, "Magnetohydrodynamic Induction Machine with Laminar Fluid Flow," Quarterly Progress Report No. 77, Research Laboratory of Electronics, M.I.T., Cambridge, Mass., April 15, 1965, pp. 218-232.

9. H. Schlichting, op. cit., p. 126.

10. Ibid., pp. 534-539.

11. Ibid., p. 539.

12. Ibid., p. 515.

13. L. P. Harris, op. cit., p. 55.

C. PRELIMINARY EXPERIMENTAL RESULTS ON AN MHD INDUCTION
   GENERATOR

A brief description of the design of a coil system for an MHD induction generator
is given in this section, and preliminary experimental results are also included. The
previous theoretical treatment of the MHD induction generator[1] is expanded to corre-
spond more closely to the experimental device by including: (a) the effects of an air gap
and conducting channel walls between the exciter and the fluid; and (b) the effects of non-
conducting side walls. An optimization of the theoretical results is described.

1. Effect of Conducting Walls and an Air Gap

A practical generator will probably have to operate on a stream of liquid metal
flowing in a duct with electrically conducting walls. Heat-transfer considerations may
require the core to be displaced from the channel. Pierson[1] has considered the prob-
lem of a finite gap but without conducting channel walls. As the power lost in the walls
is not negligible, a modification of his theory is presented here.

It is assumed in the analysis that the fluid and metal walls have the permeability of
air, and that the magnetic core has infinite permeability. The edges of the generator
are assumed to be perfectly conducting.

The model is shown in Fig. XI-6. Regions 1, 2, 3 refer to the fluid, the channel
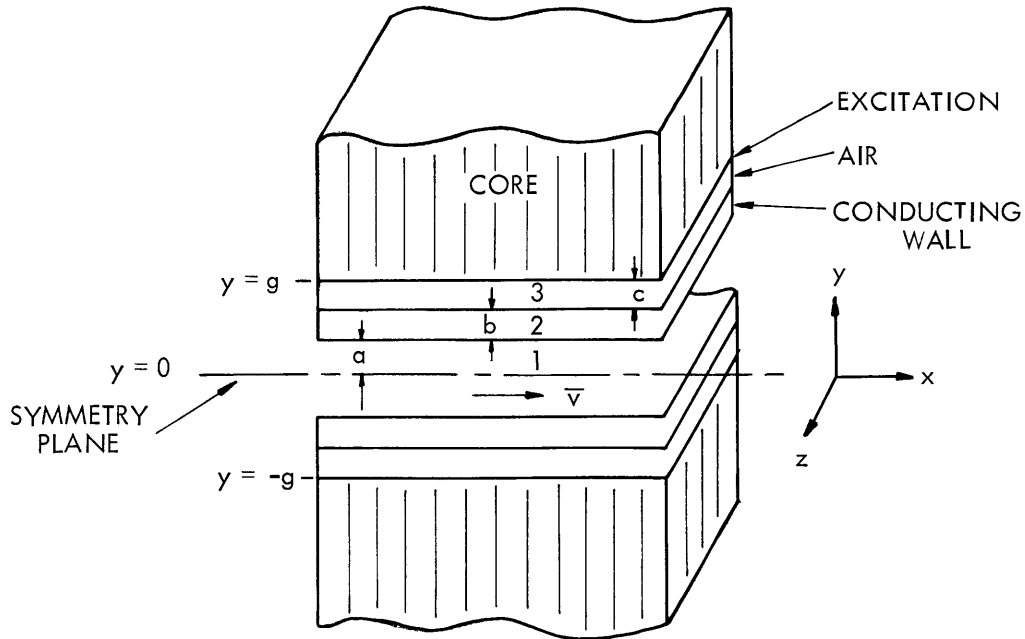wall, and the air gap, respectively. The current excitation is located at $y = g$.

Fig. XI-6. The model (conducting walls).

The device is described by Maxwell's equations with the usual MHD approximation. The analysis is simplified by the introduction of a vector and a scalar potential defined as

$$\overline{B} = \nabla \times \overline{A} \tag{1}$$

and

$$\nabla \cdot \overline{A} = \mu\sigma\phi. \tag{2}$$

Solving Maxwell's equations for these potentials and assuming a constant fluid velocity, we find that

$$\nabla^2 \overline{A} - \mu\sigma \frac{\partial \overline{A}}{\partial t} + \mu\sigma(\overline{v} \times [\nabla \times \overline{A}]) = 0 \tag{3}$$

and

$$\nabla^2 \phi = \mu\sigma \frac{\partial \phi}{\partial t}. \tag{4}$$

The current excitation is

$$\overline{K}(y=\pm g) = \text{Re} \left[NI \, e^{j(\omega t - kz)} \right] \vec{i}_z, \tag{5}$$

where N is the turns density per unit length, I is the current amplitude, and $k = 2\pi/\lambda$ is the wave number. The wave travels in the z-direction with velocity $v_s = \omega/k$.

For this case the vector potential is independent of z; thus the scalar potential, ϕ, is zero in all three regions. The equations to be solved in each region are

$$\frac{d^2 A_{z_1}}{dy^2} - \gamma^2 k^2 A_{z_1} = 0 \tag{6}$$

$$\frac{d^2 A_{z_2}}{dy^2} - \phi^2 k^2 A_{z_2} = 0 \tag{7}$$

and

$$\frac{d^2 A_{z_3}}{dy^2} - k^2 A_{z_3} = 0, \tag{8}$$

where

$$A_{z_i} = A_{z_i}(z) \, e^{j(\omega t - kz)}, \tag{9}$$

$$\gamma^2 = 1 + jsR_m \tag{10}$$

$$R_m = \frac{\mu_0 \sigma_f v_s}{k} \tag{11}$$

$$s = 1 - \frac{v}{v_s} \tag{12}$$

$$\phi^2 = 1 + jR_{m_s} \tag{13}$$

and

$$R_{m_s} = \frac{\mu_0 \sigma_s v_s}{k}. \tag{14}$$

The solution of these equations is substituted in expressions for power flow and pressure drop. The results in region 1 are

$$\langle \Delta p \rangle = \mu_0 N^2 I^2 \ell \frac{sR_m \frac{a}{g}}{1 + \left[R_{m_s} \frac{b}{g} + sR_m \frac{a}{g} \right]^2} \tag{15}$$

$$P_{s_1} = \frac{\mu_0 N^2 I^2 w \ell v_s}{kg} \frac{sR_m \frac{a}{g}}{1 + \left[R_{m_s} \frac{b}{g} + sR_m \frac{a}{g} \right]^2} \tag{16}$$

and

$$P_{m_1} = (1-s) P_{s_1}, \tag{17}$$

where w is the channel width, ℓ the length, P_{s_1} the electrical power entering region 1, and P_{m_1} the mechanical power leaving region 1. Evaluating the power entering region 2, we find that

$$P_{s_2} = \frac{\mu_0 N^2 I^2 w \ell v_s}{kg} \frac{R_{m_s} \frac{b}{g}}{1 + \left[R_{m_s} \frac{b}{g} + sR_m \frac{a}{g} \right]^2} \tag{18}$$

The total electrical and mechanical power is

$$P_s = \frac{\mu_0 N^2 I^2 w \ell v_s}{kg} \frac{R_{m_s} \frac{b}{g} + sR_m \frac{a}{g}}{1 + \left[R_{m_s} \frac{b}{g} + sR_m \frac{a}{g} \right]^2} \tag{19}$$

and

$$P_m = \frac{\mu_o N^2 I^2 w \ell v}{kg} \frac{sR_m \frac{a}{g}}{1 + \left[R_{m_s} \frac{b}{g} + sR_m \frac{a}{g} \right]^2}.$$ (20)

2. Effect of Nonconducting Walls

A conducting fluid often makes poor contact with the channel walls. For this reason, it is practical to investigate a fluid that is completely surrounded by insulating walls. Natural modes are generated by assuming current distributions that vary sinusoidally in the z-direction. The actual current distribution will be uniform in the z-direction.
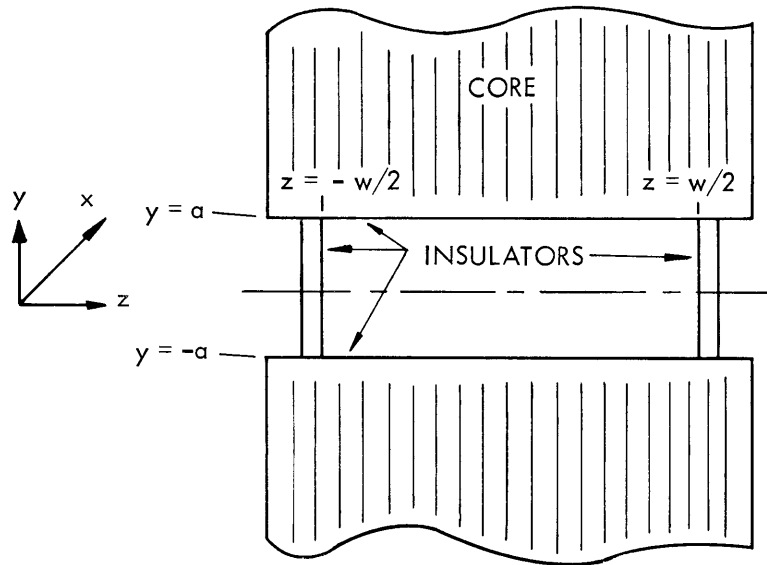
Fig. XI-7. The model (nonconducting walls).

Expanding a uniform distribution in a Fourier series, we find that only the first harmonic makes an important contribution to the pressure and power. The model is shown in Fig. XI-7. The current distribution is assumed to be

$$\underline{K}(y=\pm a) = N_n I \cos \beta k z \vec{i}_z + j\beta N_n I \sin \beta k z \vec{i}_x.$$ (21)

Following the analysis above, Maxwell's equations become

$$\nabla^2 \underline{A}_y - jk^2 sR_m \underline{A}_y = 0$$ (22)

$$\nabla^2 \underline{A}_z - jk^2 sR_m \underline{A}_z = 0$$ (23)

and

$$\nabla \cdot \overline{A} + \mu\sigma\underline{\phi} = 0, \tag{24}$$

where

$$\overline{A} = \overline{A}(y,z) \, e^{j(\omega t - kz)}. \tag{25}$$

A_x is assumed to equal zero, since it is independent of the fluid motion and not necessary in matching the boundary conditions.

The mechanical and electrical powers are

$$P_s = \frac{0.8\mu_o N^2 I^2 w \ell v_s}{ka} \cdot \frac{\dfrac{sR_m}{1 + \left(\dfrac{\lambda}{2w}\right)^2}}{1 + \dfrac{s^2 R_m^2}{\left(1 + \left(\dfrac{\lambda}{2w}\right)^2\right)^2}} \tag{26a}$$

and

$$P_m = (1-s) \, P_s. \tag{26b}$$

3. Combination of Edge and Conducting Wall Effects with a Realizable Winding

It is very difficult to make a truly sinusoidal winding. Instead, a rectangular distribution is used. Only the first harmonic of the rectangular distribution has an important effect in the power expressions. The winding that was used for the coil system has an effective turns density, N, given by

$$N = \frac{18 N_w}{\pi\lambda}, \tag{27}$$

where N_w is the number of turns per pole per phase.

The experimental generator has both of the effects previously mentioned. The pertinent power expressions with the actual winding are

$$P_s = \frac{0.8\mu_o \left(\dfrac{18 N_w}{\pi\lambda}\right)^2 I^2 w \ell v_s}{kg} \cdot \frac{R_{m_{eq}}}{1 + R_{m_{eq}}^2} \tag{28}$$

and

$$P_m = \frac{0.8\mu_o \left(\dfrac{18 N_w}{\pi\lambda}\right)^2 I^2 w \ell v}{kg} \left(\frac{sR_m \dfrac{a}{g}}{1 + \left(\dfrac{\lambda}{2w}\right)^2}\middle/ \left(1 + R_{m_{eq}}^2\right)\right), \tag{29}$$

where

$$R_{m_{eq}} = \frac{sR_m \frac{a}{g} + R_{m_s} \frac{b}{g}}{1 + \left(\frac{\lambda}{2w}\right)^2}.$$ (30)

4. Coil Design

The objective of the design is to maximize P_s, subject to a given pump constraint. Typical pump constraints are shown in Fig. XI-8. Fluid friction loss is included by using the ordinary hydrodynamic equation for turbulent flow. The channel width and length are removed as independent variables by making them functions of the wavelength.
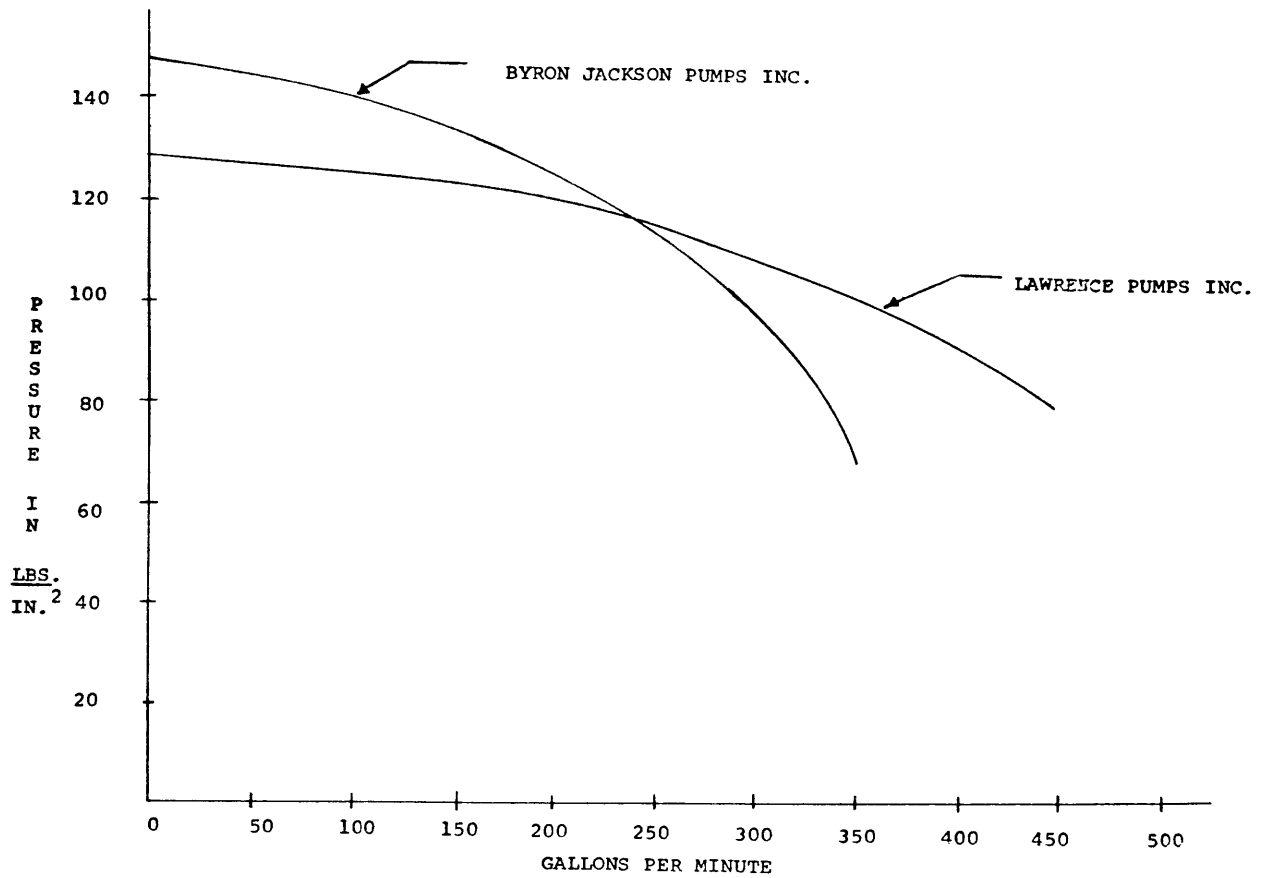

Fig. XI-8. Illustrating pump constraints.

As the upper frequency is limited by the electrical drive to 60 cps, and as it is desired that there should be zero slip at the upper frequency, the fluid velocity is constrained to
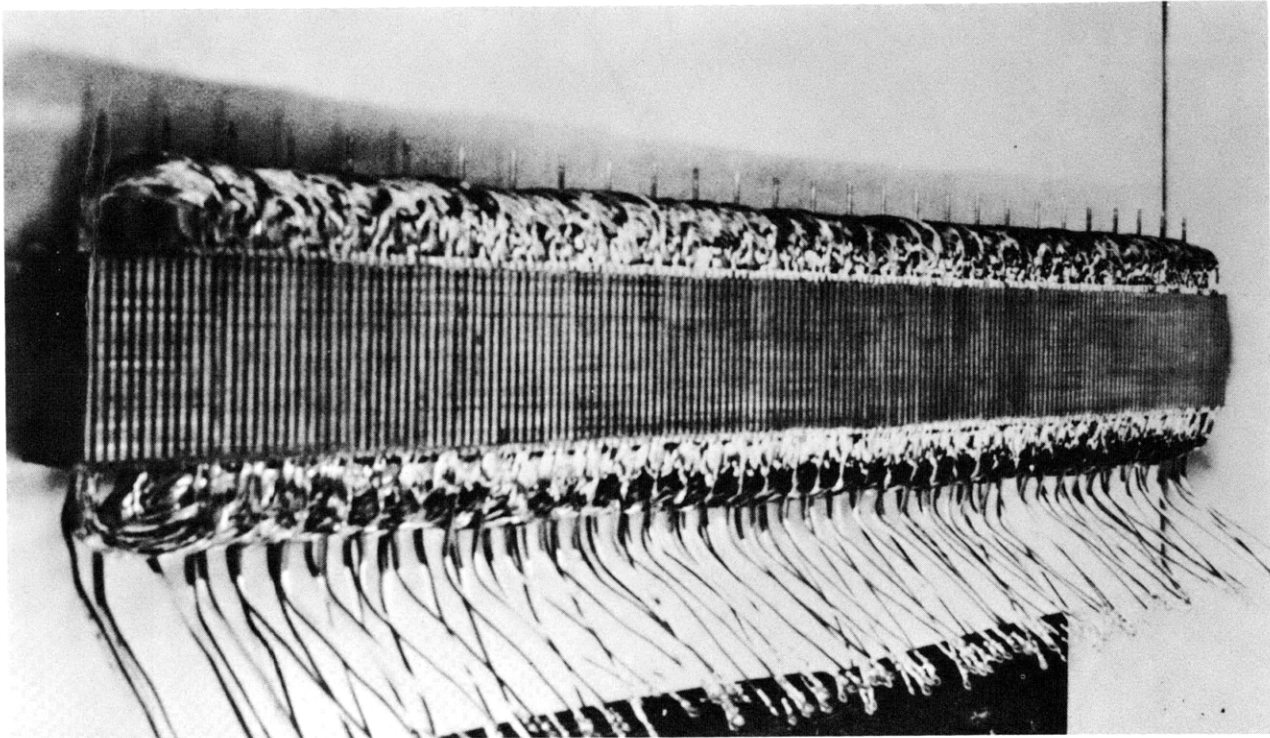
$$v_o = f_o \lambda,$$ (31)

Fig. XI-9.   Stator of the coil system.

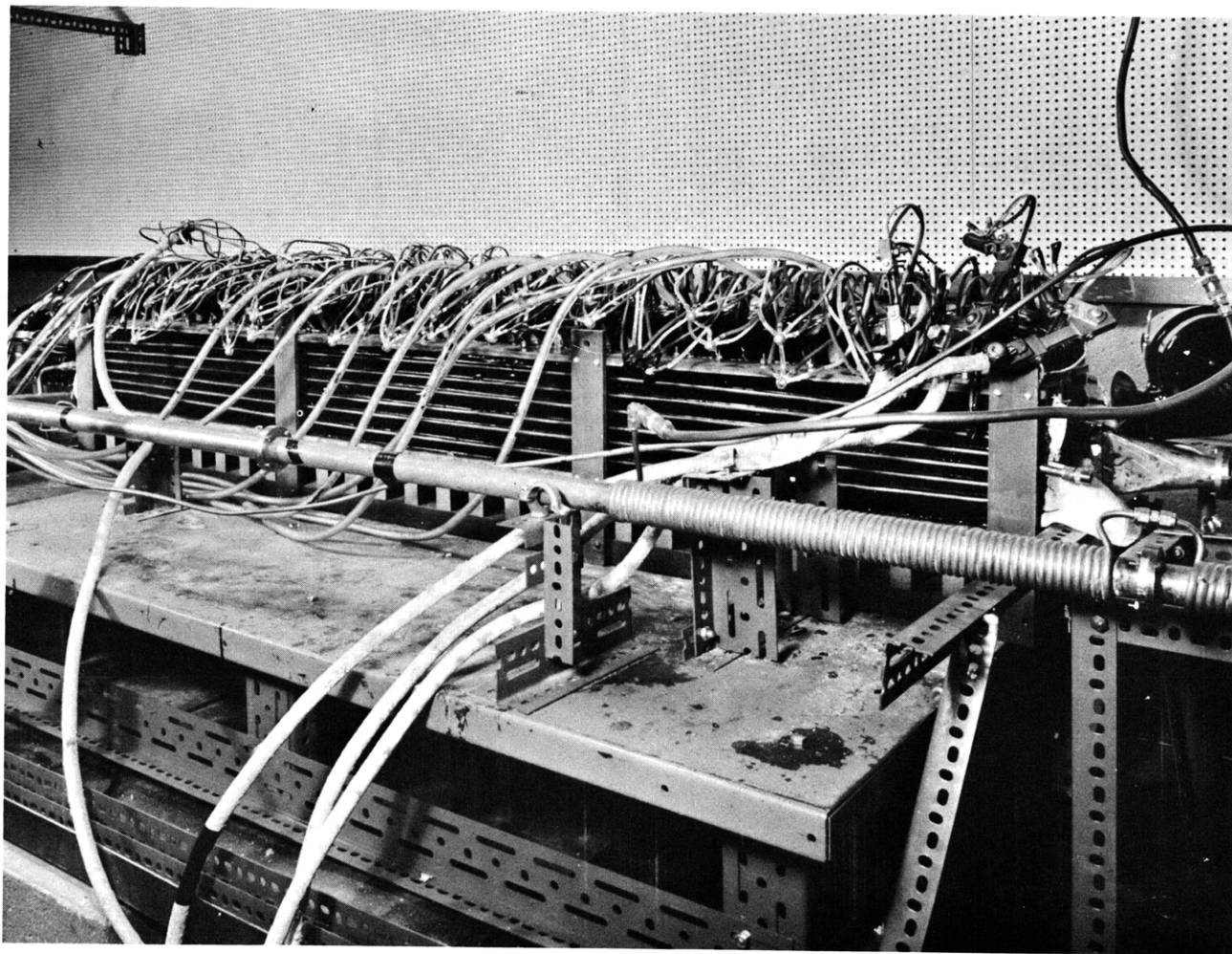Fig. XI-10 Assembled coil system coupled to the flow loop.

where f_o = 60 cps. It is then possible to maximize P_s with respect to λ, the wavelength, and a, the half-gap of the fluid.

The results of the maximization are

λ = 0.25 m

$a = b = 0.3 \times 10^{-2}$ m

w = 0.125 m

N_w = 40

I = 30 amps

v = 15 m/sec

f = 22 cps.

The choice of these parameters results in a predicted power level of P_s = 1200 watts. Photographs of the coil system are shown in Figs. XI-9 and XI-10.

5. Testing of the Coil System

The coil system described above was coupled to a low-velocity flow loop for preliminary testing. An experiment similar to that of Reid was performed. Data were obtained of the resistance per phase with the two sides of the coil system connected in parallel and with the coils operating in the brake mode. An Anderson bridge was used in the measurement. The correlation between theory and experiment was made by using

$$R_{s_n} = \frac{P_s}{6|I|^2}.$$

The close agreement between theory and experiment is shown in Figs. XI-11 and XI-12. The theoretical calculation, represented by the dashed curve, is for the case
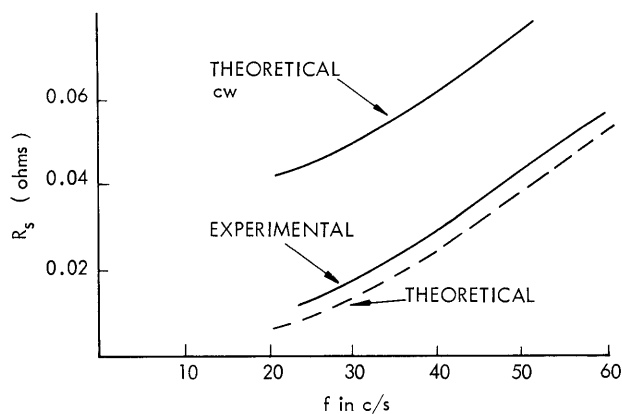

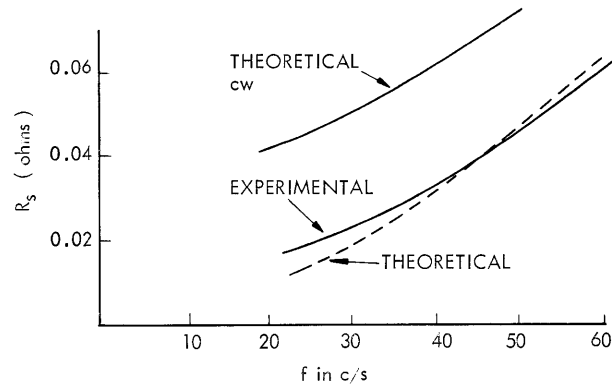Fig. XI-11.   Test results on coil system compared with theory, for v = 0 m/sec.

Fig. XI-12.   Test results on coil system compared with theory, for v = 3 m/sec.

of insulating side walls.   Performing the calculation again with conducting side walls assumed, we obtain the upper curve.   As the channel was copper with a flash-coating of nickel, it is clear that Nak does not wet nickel.

R. P. Porter, W. D. Jackson

References

1. E. S. Pierson, "The MHD Induction Machine," Sc.D. Thesis, Department of Electrical Engineering, M.I.T., 1964.

D. THERMIONIC CHARACTERISTICS OF THE (110) AND (112) DIRECTIONS
OF TUNGSTEN IN CESIUM VAPOR

This report is a condensed version of a paper presented by J. L. Coggins and R. E. Stickney at the Twenty-fifth Annual Conference on Physical Electronics, March 24, 25, and 26, 1965, at the Massachusetts Institute of Technology. A more detailed report of this work is included in the doctoral dissertation of J. L. Coggins, Department of Mechanical Engineering, M. I. T. , June 1965.

1. Introduction

Interest in the thermionic and adsorption properties of metallic surfaces has been stimulated in recent years by thermionic energy conversion and ion propulsion. Several analytical models have been proposed for describing the emission properties of metallic surfaces partially covered by alkali-metal films,[1-3] and the attributes of each have been considered critically.[4-6] It is of interest to note that these recent models are based primarily on experimental data obtained more than thirty years ago by Taylor and Langmuir.[7] Although the Taylor-Langmuir data are exceptionally reliable and complete, they do not furnish an appropriate basis for the evaluation and further development of a detailed model of emission and adsorption processes because the crystallographic structure of the tungsten specimen was not well defined.[8] For this reason, we have undertaken an experimental investigation of the dependence of thermionic emission from tungsten on crystallographic direction, temperature, and cesium arrival rate (i. e. , we wish to obtain a set of "Langmuir S-curves" for various crystallographic orientations). The results of the first stage of this investigation are presented here.

Although several investigations of the properties of alkali-metal films adsorbed on single-crystal substrates have been performed in the past, none of these fulfill completely the objective stated above. The effects of cesium on the work functions of various crystallographic directions of tungsten were determined qualitatively, in 1939, by Martin,[9] using the projection microscope technique. More recently, Webster and Read[10] have conducted similar studies of cesium on tungsten, molybdenum, tantalum, rhenium, nickel, niobium, and niobium carbide. (Potassium and rubidium were also studied on a few metals.) In addition to the results of this qualitative survey, Webster and Read also report some quantitative data on the temperature dependence of thermionic emission from the (001), (110), and (111) faces of tungsten in cesium vapor. The field emission microscope has been employed by Swanson, Strayer, and Charbonnier[11] to measure the dependence of the work function of (001) tungsten on cesium coverage.

2. Experiment

The apparatus will not be described here, since it has been covered in previous progress reports. A graph of electron emission against crystallographic direction is
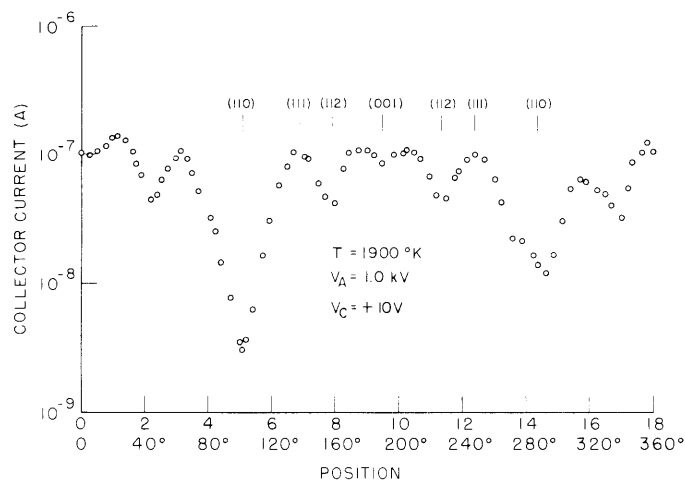
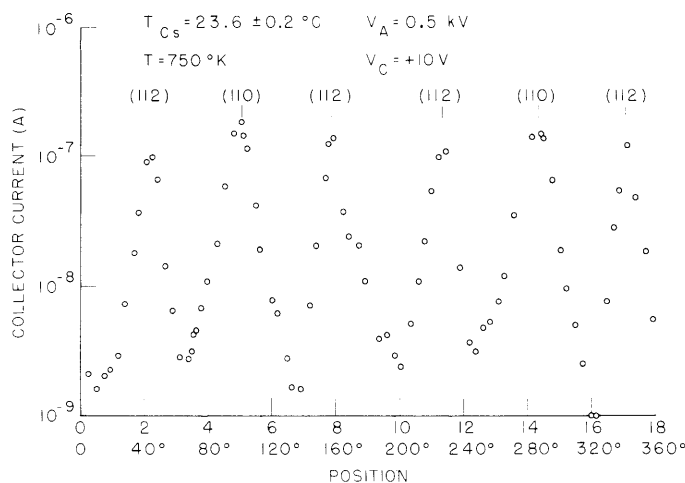Fig. XI-13.   Emission map in vacuum.

Fig. XI-14.   Emission map in cesium vapor.

presented in Fig. XI-13 for the case of clean tungsten.   This should be compared with the corresponding graph for cesiated tungsten shown in Fig. XI-13.   Note the complete reversal of the pattern.   Specifically, the (110) and (112) directions, which were emission minima for clean tungsten, become emission maxima in the presence of cesium. This is in accord with results obtained by other techniques.[9-11]   Also note that the peaks of emission at 750°K in cesium vapor are of the same order of magnitude as those at 1900°K in vacuum.

Shown in Fig. XI-15 is an S-curve measured in the (110) direction for a cesium reservoir temperature of 40°C.   Leakage currents prevented us from measuring the complete S-curve.   The measured current values have been divided by the area emitting through the slit $(2.88 \times 10^{-4}$ $cm^2)$ but have not been reduced from the experimental field conditions $(2.4 \times 10^4$ V/cm) to zero field.   The data were quite reproducible with little
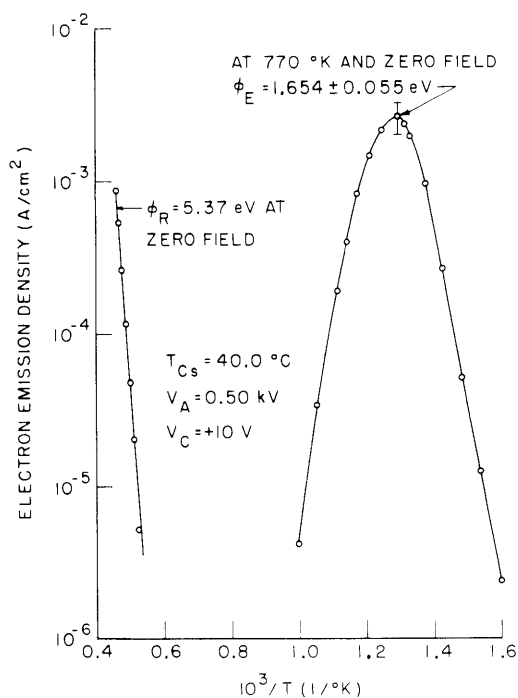
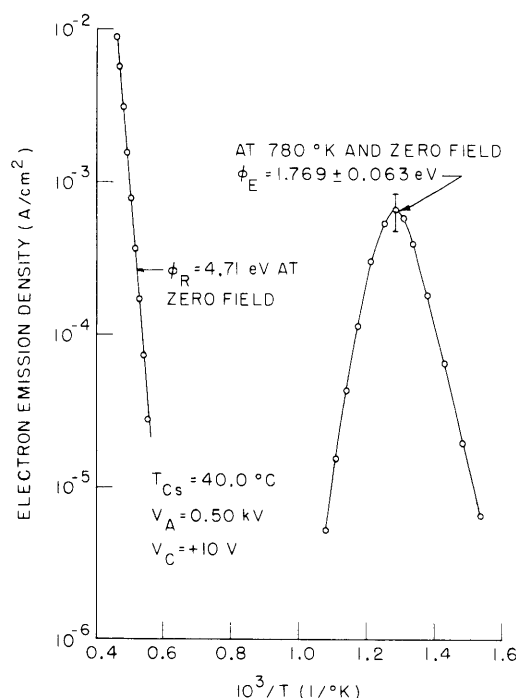Fig. XI-15. S-curve for (110) direction at 5.10 position.

Fig. XI-16. S-curve for (112) direction at 7.00 position.

scatter, except in the vicinity of the emission peak. The standard deviation from the average value of current at the peak (T = 770°K) was calculated for the 29 recordings of this S-curve and is shown in Fig. XI-15. This scatter, together with the 2.5% precision with which the filament temperature could be measured, is reflected in the error limits shown for the work function at the peak. Although the slopes, ϕ_R, of the high-temperature portions of the curves obtained for other directions were generally in good agreement with the corresponding values measured in vacuum, for some unknown reason the ϕ_R for this (110) direction is considerably higher than the value of 4.78 ev measured in vacuum. It should be emphasized that these data are for the well-defined (110) direction (i.e., position 5.10). When the high-temperature portion of the curve was displayed as a Richardson plot, it was found that the points did not form a good straight line; therefore, the Richardson slope of 5.37 ev reported in Fig. XI-15 is not reliable.

Figure XI-16 shows an S-curve taken in the (112) direction at the 7.90 position. The standard deviation shown at the peak was calculated for 10 recordings of the curve. The value of the slope of the high-temperature straight-line portion is in good agreement with the value of 4.69 ev for the (112) direction reported by Nichols[12] and the value of 4.65 ev reported by Smith.[13] An S-curve taken in the (112) direction at the 11.35 position agrees closely with the data shown in Fig. XI-16 for the 7.90 position. It should be noted that although the magnitude of the peak current for the (112) direction is less than that for the (110) direction, the peak occurs at a slightly higher temperature. This temperature relationship was also observed by Webster and Read,[10] and they believe that it was the
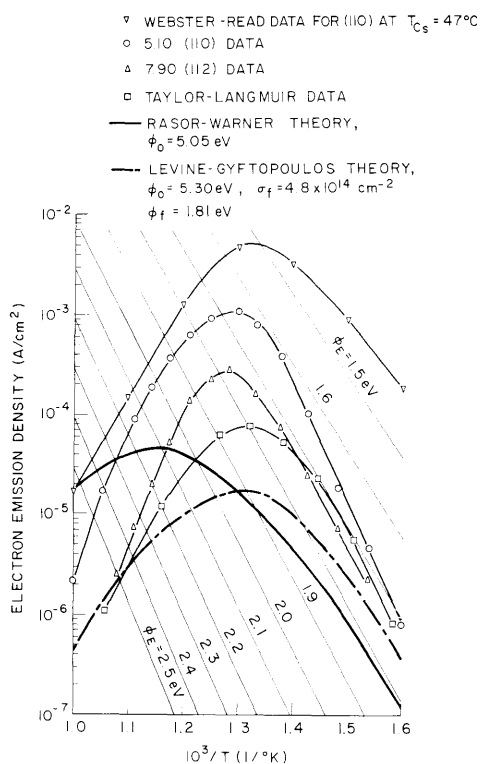
Fig. XI-17. Field-free electron emission at T_{Cs} = 40°C.

result of contamination. It appears that the data for the (112) direction are not as reliable as those for the (110) direction because there is evidence that the (112) face is extremely sensitive to contamination.[9-11] For this reason, we shall emphasize only the (110) data in the following section.

3. Experimental Results

The S-curve shown in Fig. XI-15 for the (110) direction has been replotted in Fig. XI-17 after correcting it for the zero-field condition. Also included in Fig. XI-17 are experimental curves reported by Webster and Read[10] and by Taylor and Langmuir,[7] as well as theoretical curves obtained from the Rasor-Warner[1] and the Levine-Gyftopoulos[2] models. We shall now compare each of these curves with our experimental results.

It is unfortunate that the only S-curve reported by Webster and Read[10] for the (110) direction of tungsten is at a cesium temperature of 47°C instead of 40°C. Although this temperature difference is a logical explanation for the fact that their data fall slightly above ours, the cause of the discrepancy observed at low filament temperatures is unknown.

In Fig. XI-17 we see that the Taylor-Langmuir data are approximately one order of magnitude below those measured for the (110) direction at the same cesium temperature. This indicates that their filament surface was not entirely (110) faces, as they had assumed. It is likely that the surface of the filament consisted of a variety of crystal faces having work functions both above and below the measured value of 4.62 ev.

Since the Rasor-Warner model depends strongly on the bare work function of the substrate, a valid comparison of theory and experiment cannot be made unless we know the bare work function of the (110) direction. This presents a problem because accurate measurement of the (110) work function is not possible with the tube design employed here.[12-13] If we assume Smith's estimate of 5.26 ev for the (110) direction,[13] the nearest case computed by Rasor and Warner is that for 5.05 ev. We have plotted this case in Fig. XI-17 and it is obvious that the agreement between theory and experiment is unsatisfactory. The plot of ϕ against T/T_{Cs} shown in Fig. XI-18 is an alternative means of presenting the information contained in Fig. XI-17, and we see that neither the 5.05-ev nor the 4.62-ev case of the Rasor-Warner model is satisfactory. Note that
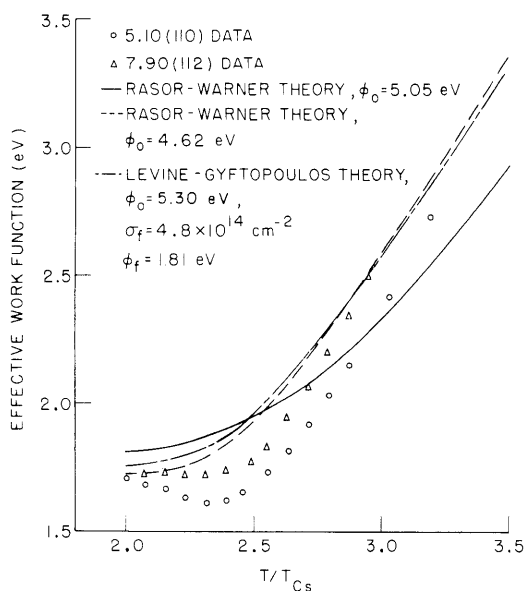
Fig. XI-18. Effective work functions at $T_{Cs} = 40°C$.

the minimum work function shown for the (110) face is 1.61 ev. The minimum work function observed by Taylor and Langmuir[7] was 1.70 ev, while the minimum work function observed by Swanson, Strayer, and Charbonnier[11] for cesium-on-tungsten was ~1.53 ev for the entire field-emission tip, and ~1.58 ev for the (001) face.

It should be recalled here that Rasor and Warner have warned that, since many oversimplifications have been used in constructing the model, one should not expect it to be valid for all possible cases.[1,4] The most severe oversimplification may be the assumption that the only properties of the substrate which influence thermionic emission in the presence of cesium are temperature and bare work function. The experimental results of Webster and Read[10] appear to indicate that other properties of the substrate, such as compatibilities of the crystallographic structures, may be influential. (For example, Webster and Read found that the (110) and (112) directions were not the strongest emitters in the case of potassium and molybdenum.

S-curves calculated from the Levine-Gyftopoulos model are more sensitive to the work function ϕ_f and the adsorbate density σ_f at one monolayer coverage than to the bare work function. Since ϕ_f and σ_f were not measured in this experiment, it is difficult to make a valid comparison of theory with experiment. The curve included in Figs. XI-17 and XI-18 is based on the values of ϕ_f and σ_f measured by Taylor and Langmuir[7] for cesium on tungsten; it is obvious that the agreement is unsatisfactory. We have not shown curves for values of the bare work function other than 5.30 ev because their theory is not very sensitive to this property. It appears that the Levine-Gyftopoulos theory cannot produce satisfactory correlation in the present case, unless we relax their assumption that ϕ_f is equal to that of bulk cesium.

4. Conclusions

The data reported here show that at moderate emitter and cesium temperatures the emission maxima for the (110) and (112) directions are much greater than those for the other (hhk) directions of tungsten. This result is consistent with those obtained by other techniques.[9-11]

Work functions calculated from measurements of electron emission are substantially lower than those predicted by the Rasor-Warner theory. In the absence of measured values of ϕ_f and σ_f or, alternatively, a knowledge of the coupling of ϕ_f and σ_f with ϕ_o, it

is impossible to make a valid comparison between the calculated work functions and those predicted by the Levine-Gyftopoulos theory.

The apparatus developed a leak before measurements at other cesium reservoir temperatures could be obtained. The tube has been repaired and we are now attempting to repeat and extend the measurements.

J. L. Coggins, R. E. Stickney

References

1. N. S. Rasor and C. Warner, J. Appl. Phys. 35, 2589 (1964).

2. J. D. Levine and E. P. Gyftopoulos, Surface Science 1, 171, 225, 349 (1964).

3. A summary of other theoretical models is presented in N. S. Rasor, "Report on the Thermionic Conversion Specialist Conference, Cleveland, Ohio, October 26-28, 1964," pp. 115-124.

4. Ibid., loc. cit.

5. J. D. Levine and E. P. Gyftopoulos, "Report on the Thermionic Conversion Specialist Conference, Cleveland, Ohio, October 26-28, 1964," pp. 125-131.

6. J. W. Gadzuk, "Report on the Twenty-fifth Annual Conference on Physical Electronics, M. I. T. , March 24-26, 1965," pp. 93-100.

7. J. B. Taylor and I. Langmuir, Phys. Rev. 44, 423 (1933).

8. Taylor and Langmuir have claimed that thermal aging of a tungsten filament produces an etched surface structure consisting of crystal planes with (110) orientation. The validity of this claim is questionable because the measured work function of 4. 62 ev is much lower than that of (110) tungsten.

9. S. T. Martin, Phys. Rev. 56, 947 (1939).

10. H. F. Webster and P. L. Read, Surface Science 2, 200 (1964).

11. L. W. Swanson, R. W. Strayer, and F. M. Charbonnier, "Report on the Twenty-fourth Annual Conference on Physical Electronics, M. I. T. , March 25-27, 1964," p. 120.

12. M. H. Nichols, Phys. Rev. 57, 297 (1940).

13. G. F. Smith, Phys. Rev. 94, 295 (1954).